**Key Points:**

- The spatial structure of oxygen deficient zones (ODZs) can be characterized at high resolution via the continuous depth profile of oxygen
- Lateral intrusions of oxygenated water into the ODZs are common, and typically isolated along the boundaries
- The eastern tropical North Pacific oxygen deficient zone is thicker, more expansive, and shifted deeper compared to the South Pacific ODZ

**Author Contributions:**
**Conceptualization:** Jarek V. Kwiecinski, Andrew R. Babbin
**Data curation:** Jarek V. Kwiecinski
**Formal analysis:** Jarek V. Kwiecinski, Andrew R. Babbin
**Investigation:** Jarek V. Kwiecinski, Andrew R. Babbin
**Methodology:** Jarek V. Kwiecinski, Andrew R. Babbin
**Software:** Jarek V. Kwiecinski
**Validation:** Jarek V. Kwiecinski, Andrew R. Babbin
**Visualization:** Jarek V. Kwiecinski, Andrew R. Babbin
**Writing – original draft:** Jarek V. Kwiecinski, Andrew R. Babbin
**Writing – review & editing:** Jarek V. Kwiecinski, Andrew R. Babbin

# A High-Resolution Atlas of the Eastern Tropical Pacific Oxygen Deficient Zones

**Jarek V. Kwiecinski[1,2,3]** and **Andrew R. Babbin[1]**

[1]Department of Earth, Atmospheric and Planetary Sciences, Massachusetts Institute of Technology, Cambridge, MA, USA, [2]Department of Civil and Environmental Engineering, Massachusetts Institute of Technology, Cambridge, MA, USA, [3]Now at Division of Geological and Planetary Sciences, California Institute of Technology, Pasadena, CA, USA

**Abstract** Oxygen deficient zones (ODZs) are important biogeochemical provinces of the global oceans wherein standing dissolved oxygen concentrations decrease to nanomolar levels. Despite their confinement, these regions are disproportionally important to the ocean's role in modulating Earth's climate through the interactions between the marine nitrogen cycle and that of carbon. Moreover, the spatial domain of low oxygen regions of the ocean is predicted to change as a consequence of ocean warming, increased stratification, and changes in circulation and productivity. However, the expanse of the modern ODZs is poorly resolved due to a dearth of direct sampling compounded with errors that arise in the processing and gridding of the sparse measurements that do exist. Here, we take a novel approach to map the horizontal and vertical extent of the two major ODZs of the eastern tropical Pacific via analysis of meter-scale resolution electrode sensors from both ship casts and Argo profiles, rather than from discretized bottle measurements. The resulting three-dimensional data product is based on a compendium of nearly 15 million measurements taken across three decades and provides the precise locations of low oxygen water, elucidating the ODZs' three-dimensional structures. It can be utilized by researchers to validate models, plan cruise occupations, and as a comparison for future change. Calculations made with this high-resolution atlas also provide the volumes, layers of maximal areal extent, and other descriptive statistics for both Pacific ODZs. Finally, the atlas reveals fine-scale features of oxygenated water mass intrusions and regional differences across these anoxic zones.

**Plain Language Summary** Using high resolution, meter-scale profiles of oxygen, we derive the locations and fine-scale structure of the Pacific Ocean's oxygen deficient zones. These zones are regions of the lowest oxygen concentrations in the global ocean and host anaerobic metabolisms that result in the loss of bio-available nitrogen and the emission of the potent greenhouse gas, nitrous oxide. This new approach, compiling tens of thousands of profiles and over 15 million individual measurements, is a leap forward in the representation of these climate critical regions as the method does not rely on arbitrarily defining a sensor-dependent detection limit. Instead, the vertical gradient in the measurements is used to not only identify the layers of functional anoxia but also to quantify the intrusion of oxygenated waters into these zones. The resulting gridded data set, the most reliable produced to date, is freely available for scientists and the general public to use to in their research and policy-making efforts. This comprehensive data set can moreover be used in the validation of climate models.

## 1. Introduction

Oxygen deficient zones (ODZs) are persistent regions of the ocean in which rapid heterotrophic respiration and poor ventilation result in oxygen ($O_2$) concentrations below detection by conventional means (Margolskee et al., 2019). Two of the largest ODZs occur at pelagic depths within the Eastern Tropical North and South Pacific (ETNP and ETSP), where dissolved $O_2$ concentrations <10 nmol kg$^{-1}$ have been observed (Thamdrup et al., 2012). Within these regions, anaerobic microbial metabolisms, including denitrification and anammox, are possible, causing ODZs to have a significant impact on global biogeochemical cycles of nitrogen, and by consequence, carbon. ODZs generate roughly half of marine nitrous oxide emissions despite occupying only 0.35% of the ocean's volume (Codispoti, 2010; Karstensen et al., 2008) and are responsible for 20%–40% of marine bio-available nitrogen loss (Brandes & Devol, 2002; DeVries et al., 2013). In addition, significant oxygen loss from the oceans has been observed in the past 50 years (Schmidtko et al., 2017; Stramma et al., 2008), and climate models generally predict further deoxygenation due to thermal effects on solubility (Cabré et al., 2015). Predicted trends for ODZs are more complex, however, as increased stratification in the tropics can curtail localized
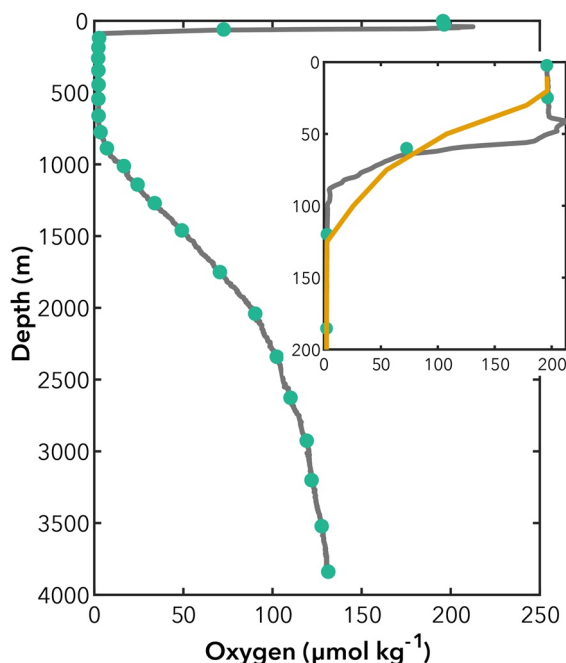
**Figure 1.** Oxygen profile from 14°N 110°W in the ETNP ODZ constructed from Winkler titration (teal points) or Clark-type electrode (gray line) measurements. Data are from the P18 GO-SHIP occupation in November 2016. Because Winkler titration measurements were made at lower vertical resolution, interpolated gridded profiles based on this data (orange line denotes standard WOA gridding) overestimate the depth at the bottom of the upper oxycline (i.e., the top of the ODZ). The sensor-based profile contains measurements made at 24 Hz averaged to a 1-meter vertical resolution, and more accurately represents the steepness of the vertical oxygen gradient in the upper oxycline and the depth at the top of the ODZ.

upwelling, which would yield less primary productivity and greater $O_2$ concentrations in the interior (Ito & Deutsch, 2013). Moreover, models struggle to accurately reproduce modern ODZ boundaries (Cabré et al., 2015). Additional observational data are needed to validate current global biogeochemical models and improve model predictions by enhancing the current understanding of physical and biogeochemical mechanisms that control the extent of ODZs (Breitburg et al., 2018).

Previous attempts to characterize the structure of ODZs have largely relied on gridded datasets with low vertical resolution. Paulmier and Ruiz-Pino (2009) estimated the thickness and horizontal area of the world's oxygen minimum zones (OMZs) using World Ocean Atlas (WOA) 2005 data. OMZs were divided into an upper oxycline, in which $O_2$ concentrations decrease rapidly with depth, an anoxic core with $[O_2] < 20$ μmol $L^{-1}$, and a lower oxycline in which $O_2$ concentrations gradually increase below the core. Since most marine profiles contain an oxygen minimum and thus a corresponding oxygen minimum zone, the use of OMZ to refer to the large anoxic regions described by Paulmier and Ruiz-Pino (2009) can cause confusion. For clarity, we opt to use the oxygen deficient zone (ODZ) terminology throughout this paper to distinguish between ubiquitous oxygen minima and the locations of below-detection oxygen concentrations where fixed nitrogen loss tends to occur.

Similar attempts to characterize the ODZ can be fraught with errors in the estimated boundaries of these layers, as current and past WOA data incorporate only bottle measurements of $[O_2]$ collected at few depths within the ODZ. This sparse vertical resolution is insufficient to accurately identify the boundaries of important features like the upper oxycline, which occupies a narrow band of the water column (Farías et al., 2009) and supports significant nitrous oxide ($N_2O$) production (Arévalo-Martínez et al., 2015; Babbin et al., 2015). Indeed, when using the lower vertical resolution of bottle measurements, and then interpolating these to a standardized grid, the steepness of the oxycline and the depth of ODZ onset become obscured (Figure 1).

Finally, the reliance on bottle measurements introduces errors associated with the Winkler titration, a method for determining $O_2$ concentrations that is affected by interferences with iodate (G. T. F. Wong & Li, 2009) and nitrite (Revsbech et al., 2009), as well as possible contamination of samples with $O_2$ during sampling and analysis (Revsbech et al., 2009). These shortcomings illustrate the need to incorporate additional, higher spatial resolution data to fully map the extent of the ODZs.

Recent advances in optical and electrochemical oxygen sensors have allowed for the collection of $O_2$ measurements at the same vertical resolution as standard CTD data (Uchida et al., 2010). Sensor measurements do not require sampling that can cause $O_2$ contamination, and the electrical signals or changes in fluorescence used to measure $O_2$ concentrations can be recorded at very high resolutions (Revsbech et al., 2009). Still, these data have not been included in the WOA because of issues including sensor signal drift and calibration offsets that introduce uncertainty when measuring near-zero oxygen (Garcia et al., 2019). Despite this, new calibration methods are available that address some of these issues. Profiling floats, like those deployed by the Argo program, provide vast amounts of biogeochemical data that are needed to effectively constrain the extent of ODZs (Breitburg et al., 2018). Optode sensors mounted on profiling floats can be calibrated using repeated measurements of atmospheric $O_2$, a technique that has been used to quantify the drift in a sensor's $O_2$ sensitivity before and during a float's multi-year deployment (Bittig & Körtzinger, 2015; Bushinsky et al., 2016; Johnson et al., 2015). Pre-deployment drift greatly exceeds that observed in situ, where near-surface optode $[O_2]$ measurements are largely stable (Bittig et al., 2018). Drift is also minimal in anoxic waters, where measured concentrations change linearly at rates with absolute values $<0.5$ μmol $kg^{-1}$ $yr^{-1}$ (Johnson et al., 2019). Though these rates are quite low, the long duration of profiling float deployments means that measured ODZ $[O_2]$ could deviate significantly by the end of deployment from the nanomolar levels observed with lower detection limit sensors (Revsbech et al., 2009;

Thamdrup et al., 2012; Tiano et al., 2014). Correction schemes, like that proposed by Johnson et al. (2019), have been used to account for this issue, as well as the <1 µmol kg$^{-1}$ calibration offset that affects many optode sensors.

Sensors widely used on CTDs, like the Seabird SBE43 Clark-type electrode, also have limited accuracy in anoxic environments because of their high detection limit (1–2 µmol kg$^{-1}$). Electrode sensors can also drift and plastics in the sensors can leach oxygen into the water column after being exposed to the atmosphere between casts (Thamdrup et al., 2012). The detection limit and drift issues can be accounted for by zero-calibrating SBE43 data against measurements from more accurate switchable trace oxygen (STOX) sensors (Bristow et al., 2017; Thamdrup et al., 2012). However, this calibration is rarely performed and the time required to conduct individual STOX oxygen measurements makes the STOX sensor impractical for the construction of high resolution [O$_2$] profiles. Therefore, parameters other than absolute oxygen concentrations are needed to interpret the vast amount of data available from Clark-type electrodes and use it to evaluate the extent of ODZs.

This study combines tens of thousands of high vertical resolution oxygen profiles from CTD sensors and Argo floats to map the ODZs in the ETNP and ETSP. Instead of identifying these zones by defining an a priori concentration threshold or attempting to correct measured concentrations, the core of the ODZ is defined as the region in which the vertical gradient of [O$_2$], d[O$_2$]/dz, collapses to zero. This corresponds to the layer of the water column in which [O$_2$] is reduced to its minimum, a subsistence threshold that represents the minimum amount of oxygen required to support aerobic metabolism (Zakem & Follows, 2017). Significant empirical evidence (Bristow et al., 2016, 2017; Dalsgaard et al., 2014; Thamdrup et al., 2012; Tiano et al., 2014) suggests that this threshold occurs at nanomolar concentrations, magnitudes below the detection and calibration limit of most commonly utilized sensors. Importantly, because of the high precision of widely deployed optode and CTD oxygen sensors, the use of d[O$_2$]/dz allows regions with such low concentrations to be identified without regard for calibration issues that affect reported absolute concentrations. The extensive geographical coverage of sensor measurements and their high vertical resolution permits the mapping of these regions to produce a detailed three-dimensional representation of the Pacific ODZs.

## 2. Methods

### 2.1. Data Sources and Acquisition

CTD data were downloaded from the Rolling Deck to Repository (R2R) and the CLIVAR and Carbon Hydrographic Data Office (CCHDO) within bounding boxes extending far beyond the current estimated boundaries of the Pacific ODZs (Paulmier & Ruiz-Pino, 2009; Figure S1 in Supporting Information S1). All CTD oxygen, temperature, and salinity measurements added to these repositories by April 2019 were included in our ODZ maps. We used the processed Seabird CTD data files available on R2R, which contain CTD measurements generally binned at a 1 dbar vertical resolution. The CCHDO database contains CTD data binned at a 2 dbar vertical resolution or better. Additional O$_2$, temperature, and salinity data were downloaded from Argo floats that recorded measurements within the bounding boxes between January 2000 and August 2021. This included measurements made with Clark-type electrodes or optode sensors. The vertical resolution of Argo data varied from <2 dbar to ~50 dbar. The final database contained 10,079 CTD profiles and 14,605 Argo profiles, amounting to nearly 15 million O$_2$ measurements collected throughout the Eastern Pacific.

### 2.2. Data Processing

Initial data processing was conducted in the R software environment (The R Foundation, Vienna, Austria). After removing anomalous salinity, temperature and oxygen measurements (defined as salinity >40 or <30, temperature <−5 or >50°C, and [O$_2$] <−10 or >400 µmol kg$^{-1}$), data collected on the down and up casts of CTD profiles were separated. Data from the upcast were selected for further analysis except in cases where more measurements were collected on the downcast, although in practice few profiles reported complete up and downcasts. Upcasts were chosen over downcasts when sufficient data were available because the Clark-type electrodes on CTDs produce more stable measurements after spending more time in the water column (Tiano et al., 2014) and upcasts tend to be slower in practice due to additional drag on the CTD package and closing of associated bottles. This reduces the impact of any residual oxygen leaching from sensor materials on the measured oxygen gradient. Argo floats equipped with O$_2$ sensors collect data as they rise to the surface after descending to a profiling depth of 2 km (Argo Data Management Team, 2021). Argo upcasts were combined with the CTD casts for further analysis.

With this data set assembled, we first converted measured practical salinity to absolute salinity and in situ temperature to conservative temperature using the TEOS-10 equations of state (IOC et al., 2010). These conversions were necessary to calculate potential density using MATLAB code developed for the Gibbs-SeaWater (GSW) Oceanographic Toolbox (McDougall & Barker, 2011). The same toolbox and equations were used to determine potential density, which we report in sigma notation, that is, $\rho - 1,000$ kg m$^{-3}$. Following the density calculations, we smoothed the data to calculate the vertical O$_2$ gradient by fitting a cubic spline through each Argo and CTD O$_2$ profile. The derivative of the oxygen spline with respect to pressure (our preferred depth coordinate) was then calculated to determine d[O$_2$]/dz. For CTD profiles, the mean values of latitude, longitude, temperature, salinity, [O$_2$], potential density, and d[O$_2$]/dz were then calculated in 20 dbar bins and stored for later processing. Our rationale for selecting this bin width is discussed further in Section 2.3. Many Argo profiles contained depth layers with vertical resolutions sparser than this bin size. To addresses this, we used cubic spline interpolants to estimate [O$_2$], d[O$_2$]/dz, temperature, salinity, and potential density at a 20 dbar vertical resolution in depth layers where Argo data were available at a resolution better than 60 dbar. Depth layers with insufficient resolution were omitted. Now assembled, the binned data were used to evaluate the three-dimensional structure of the Pacific ODZs in depth and density space.

### 2.3. ODZ Identification and Grid Resolution Selection

We defined the ODZ as the depth layer where the vertical oxygen gradient was near zero and [O$_2$] was less than 5 µmol kg$^{-1}$. Notably, these criteria captured the ODZ regardless of the sensor calibration and the minimum oxygen concentration specific to each sensor. To determine the range of d[O$_2$]/dz values that could be considered "near zero," we randomly selected 50 Argo and 50 CTD unbinned oxygen profiles that we deemed to be part of the ODZ by visual inspection (profile locations in Figure S2 of Supporting Information S1). These profiles shared three common characteristics: an upper oxycline where [O$_2$] decreased precipitously with depth from saturation levels to a minimum <5 µmol kg$^{-1}$, a thick depth layer corresponding to the ODZ's core where [O$_2$] remained at this anoxic minimum, and a lower oxycline where [O$_2$] increased with depth below the ODZ core at a rate slower than in the upper oxycline. In all of these training profiles, it was possible to identify the depth at the top of the ODZ core visually because of the steepness of the upper oxycline. The transition to the lower oxycline was often less obvious so we used a piecewise linear regression algorithm to locate this switch-point (Muggeo, 2008). We used these bounds on the ODZ's vertical extent to determine the range of d[O$_2$]/dz values that are measured in functionally anoxic water masses where we expect the true value of the vertical oxygen gradient to be zero.

To establish d[O$_2$]/dz thresholds indicating the presence of an ODZ, we first fit cubic splines through each of the training profiles to estimate the vertical oxygen gradient. Then, we binned these derivatives as described in Section 2.2 at 5, 10, and 20 dbar resolutions. Figure S3 in Supporting Information S1 shows how the distributions of d[O$_2$]/dz within the identified ODZ core and the lower oxycline varied with bin size. There is considerable overlap in these distributions for the 5 dbar bins that decreases with bin size, indicating that sensor noise limits the resolution at which the ODZ can be reliably distinguished from the lower oxycline using a derivative threshold alone. Higher levels of smoothing and lower resolutions reduced this overlap, limiting the possibility that anoxic waters are falsely detected in the lower oxycline (Figure S4 in Supporting Information S1). However, too much smoothing can bias the results by obscuring features, including transitions between the oxyclines and the ODZ (Figure 1). Hence, we did not repeat this analysis for bin widths larger than 20 dbar and selected the d[O$_2$]/dz threshold based on training profile data binned at this resolution. For the binned CTD data, the 2.5th and 97.5th percentiles of d[O$_2$]/dz in the ODZ were −0.00773 and 0.0105 µmol kg$^{-1}$ dbar$^{-1}$ respectively. The corresponding values for the Argo training data were −0.0113 and 0.0125 µmol kg$^{-1}$ dbar$^{-1}$. Different thresholds were used for CTD and Argo data because CTDs and Argo floats use different sensor technologies, each with different noise characteristics that affect O$_2$ gradient measurements. These numerical bounds were used with the entire binned data set created in Section 2.2 to find every measured depth, density, latitude and longitude that was within the ODZ.

### 2.4. Validating ODZ Detections Using STOX O$_2$ Measurements

The d[O$_2$]/dz threshold developed in the previous section is based on profiles that have all the defining characteristics of an ODZ. Though there is some overlap in the range of measured d[O$_2$]/dz values located in the lower oxycline or the ODZ core, our criterion largely selects for observations where the [O$_2$] concentration was

at its minimum. Given existing theoretical and observational evidence (Bristow et al., 2016, 2017; Dalsgaard et al., 2014; Thamdrup et al., 2012; Tiano et al., 2014; Zakem & Follows, 2017), we believe this minimum corresponds to the functionally anoxic, nanomolar $O_2$ concentrations previously observed throughout ODZs. To further illustrate this point, we gathered data from cruises where concurrent SBE43 and STOX $[O_2]$ measurements were made at six locations in the ETNP ODZ. We calculated $d[O_2]/dz$ for the SBE43 profiles using methods outlined above and compared this vertical gradient to the STOX $[O_2]$ measurements (Garcia-Robledo et al., 2017; Tiano et al., 2014). We then plotted the distribution of STOX $[O_2]$ values where the SBE43 $d[O_2]/dz$ met our criterion to determine what range of $O_2$ concentrations are observed in this low vertical gradient regime.

### 2.5. Mapping the ODZ's Three-Dimensional Structure

To study the ODZ's three-dimensional structure, we mapped all the points within the ODZ onto a grid with $0.5° \times 0.5° \times 20$ dbar grid cells. First, we calculated the total number of points satisfying our ODZ conditions that fell within each grid cell. We then divided these values by the total number of $[O_2]$ measurements that were made in each grid cell to determine the fraction of measurements within the ODZ. This value, or fODZ, accounted for the wide variation in sampling intensity across the ODZ, as not all regions of the Eastern Tropical Pacific were sampled at the same spatiotemporal resolution. Moreover, the value of fODZ itself reflects the variability of the ODZ over time across samples. We repeated this process in potential density space with a vertical resolution of 0.1 kg m$^{-3}$. Finally, we generated three-dimensional arrays containing the values fODZ within each depth or density grid cell. We packaged these arrays into netCDF files (Data Sets S1 and S2) that used depth or density as the vertical dimension to facilitate further analyses. These netCDFs also included the mean values of $[O_2]$ and $d[O_2]/dz$ in each grid cell.

We used the fODZ metric to calculate the ODZ's volume in the ETNP and ETSP and to assess how this volume was distributed across depth and density layers. First, we estimated the value of fODZ in grid cells where there were no $[O_2]$ measurements in the database using Data-Interpolating Variational Analysis (DIVA). DIVA is a software package that harnesses the variational inverse method and finite element analysis to interpolate 2-dimensional oceanographic data (Troupin et al., 2012). DIVA importantly takes into account coastlines and ocean bathymetry and supports several methods to calculate the error in the interpolation. We generated interpolated fields of fODZ for each depth and density layer following procedures outlined in the DIVA user manual (Troupin et al., 2013). We also calculated errors using DIVA's almost-exact error method, a computationally efficient algorithm that reasonably approximates the error obtained from more rigorous theoretical calculations (Beckers et al., 2014). The interpolated fODZ depth and density layers as well as the corresponding error fields are available in netCDF files (Data Sets S3 and S4).

We used the interpolated values of fODZ to calculate the areal extent of anoxic water $A$ in each depth or density layer $k$ for the ETSP and ETNP:

$$A_k = \sum_j \sum_i a_{ijk} \ \text{fODZ}_{ijk} \tag{1}$$

In Equation 1 above, $a_{ijk}$ is the horizontal areal extent of grid cell $ijk$ at latitude and longitude $ij$ and depth or density layer $k$. The uncertainty in $A_k$ was calculated as

$$\delta A_k = \sqrt{\sum_j \sum_i a_{ijk}^2 (\delta \text{fODZ}_{ijk})^2} \tag{2}$$

in which $\delta \text{fODZ}_{ijk}$ is the error in $\text{fODZ}_{ijk}$ calculated by DIVA. We also used the values of $A_k$ for each depth layer to calculate the total volume $V$ of the ODZs by summing the $A_k$ from each hemisphere and multiplying this result by $\Delta z$, the uniform vertical bin width of 20 m. The uncertainty in $V$ was calculated as

$$\delta V = \Delta z \sqrt{\sum_k (\delta A_k)^2} \tag{3}$$

We separately estimated the error in the volume due to possible false detections of anoxic water in the lower oxycline (see Section 2.3). This excess volume was calculated as

$$V_{\text{excess}} = z_{\text{excess}} \sum_j \sum_i a_{ij} \ \text{fMAX}_{ij}$$

(4)

Here, $z_{\text{excess}}$ is the mean thickness of ODZ layers detected in the lower oxycline of the 100 training profiles selected in Section 2.3. This value was 42 dbar when using a 20 dbar binning resolution, meaning that our method on average overestimates the thickness of the ODZ by this amount. The fraction $\text{fMAX}_{ij}$ is the maximum value of the interpolated fODZ field across all depth layers in the column of grid cells at position $ij$. This is an approximation for the fraction of profiles that, if collected at this location, would intersect the ODZ at any point. It is thus a useful metric by which to weight the areas $a_{ij}$ to ensure that our calculation only accounts for the portions of each grid cell that were part of the ODZ. The values of $\text{fMAX}_{ij}$ are included in the Data Set S3. A similar maximal projection of fODZ created using the interpolated density layers is included in Data Set S4.

### 2.6. Gridded Two-Dimensional Summary Statistics

To further characterize the ODZ's structure, we calculated summary statistics on a two-dimensional grid with $0.5° \times 0.5°$ grid cells. For each binned CTD and Argo profile that intersected the ODZ, we calculated the depth at the top of the ODZ, $z_{\text{top}}$. Then, we assigned to each grid cell the mean value of $z_{\text{top}}$ calculated from all the profiles within that grid cell. This metric was useful to identify where the ODZ extended upwards into shallow waters just below the mixed layer, constraining the volume of water that could support fisheries or other aerobic life. $N_2O$ produced near the top of the ODZ's shallowest layers could also more easily reach the atmosphere (Babbin et al., 2020), especially where coastal upwelling causes supersaturation of surface waters with $N_2O$ above the ODZ (Arévalo-Martínez et al., 2015). Densities at the top of the ODZ were gridded in the same fashion and the grids containing $z_{\text{top}}$ and these densities were added to the depth and density netCDFs (Data Sets S1 and S2).

We also determined the thickness of the ODZs using the same set of binned CTD and Argo profiles. After determining the number of depths in each profile found to lie within the ODZ, we multiplied this value by the bin width and gridded it using the same method as for $z_{\text{top}}$. The thickness grid was added to the depth-based netCDF (Data Set S1). For certain profiles, Argo measurements were collected at too low a resolution to bin the $O_2$ data at 20 dbar. In these cases, thickness may be underestimated as we did not interpolate through depth layers where there were insufficient data. Consequently, no ODZ could be identified in these missing bands.

### 2.7. Offset Between Up and Down Casts

Both electrochemical and optode sensors do not respond instantaneously to changing conditions in the water column. $O_2$ molecules must diffuse through boundary layers and sensor membranes before concentrations are measured. This sensor lag affects the depth assigned to $[O_2]$ measurements as a sensor moves through the water column to construct an $[O_2]$ profile (Bittig & Körtzinger, 2017; Edwards et al., 2010). Consequently, sensor lag introduces some error in the position of the ODZ features identified in this study which we estimate here. As a case example of how sensor lag can impact the estimated depth at the top of the ODZ, 277 CTD casts were completed aboard the *R/V Falkor* at 14°N, 110°W from 6–9 July 2018. The casts were completed by repeatedly and continuously lowering a CTD with a Seabird SBE43 oxygen electrode into the water column and returning it to the surface. The cast speed was approximately 60 m min$^{-1}$, and generally achieved maximum depths of 200 m. 272 casts were deep enough to resolve the full upper oxycline and enter the ETNP ODZ core; $z_{\text{top}}$ was estimated for each of these up and downcasts. Up and downcast profiles often suggest different depths for the top of the ODZ (Edwards et al., 2010), with the true location of this feature lying between estimates made using either profile (Figure S5a in Supporting Information S1). We calculated the vertical offset ($11.2 \pm 1.6$ dbar) in $z_{\text{top}}$ as the difference between the up and downcast estimates, representing the uncertainty in the depth at the top of the ODZ induced by this sensor's lag (Figure S5b in Supporting Information S1).

To develop a more comprehensive estimate for the uncertainty in $z_{\text{top}}$, we estimated this value for all CTD profiles where both up and downcasts were reported and the data traversed the upper oxycline. We then calculated the vertical offset in $z_{\text{top}}$ as the difference between the up and downcasts. The mean value of this offset provides the combined uncertainty in the depth at the top of the ODZ induced by sensor lag and our methodology. For Argo floats, only upcasts are reported because the floats record data as they ascend from their profiling depth to the surface. Thus, we estimated the uncertainty due to sensor lag alone using lag times for optodes and common

float velocities reported in the literature. Floats rise at ~10 cm s$^{-1}$ (A. P. S. Wong et al., 2020) and are subset to a sensor lag of 60–95 s (Bittig & Körtzinger, 2017). This translates to a potential offset of 6–9.5 m too shallow.

### 2.8. Gap/Intrusion Analysis

Many of the assembled oxygen profiles had local oxygen maxima, or O$_2$ intrusions, at depths between the upper and lower oxyclines. These features are similar to the secondary oxygen maxima identified by Margolskee et al. (2019), who used their occurrence to investigate the water masses that ventilate the Eastern Pacific ODZs. To support future analyses of ODZ ventilation, we identified all the O$_2$ intrusions in our data set. We defined these intrusions to be the oxygenated layers in each O$_2$ profile that were bounded above and below by ODZ layers as identified in Section 2.3. Then, we mapped all the points that fell within these intrusions onto the three-dimensional grids used for ODZ mapping in Section 2.4. For every grid cell, we calculated an intrusion rate IR defined as

$$IR = \frac{n_I}{n_I + n_{ODZ}} \tag{5}$$

in which $n_I$ and $n_{ODZ}$ are the number of points that fell within an intrusion or the ODZ in each grid cell respectively. Though sensitive to the number of observations made in each grid cell, this metric was useful in identifying regions that were consistently part of an O$_2$ intrusion and therefore potentially important to the ODZ's ventilation. We included the intrusion rate in the depth and density netCDFs (Data Sets S1 and S2).

## 3. Results and Discussion

### 3.1. Uncertainty in the Position of ODZ Features Due to Sensor Lag

Only 401 profiles contained both up and downcasts that resolved the top of the ODZ. While upcasts were selected where possible, the vast majority of reported profiles were downcasts. The mean offset between CTD up and downcasts was 30 ± 3 (SE) dbar (median 21 dbar) and the values of $z_{top}$ estimated from downcasts were almost always greater than or equal to those estimated from upcasts (Figure S5c in Supporting Information S1). The top of the ODZ may appear deeper in downcasts because oxygen must diffuse through the membrane surrounding the sensor's core electrode. This diffusion can take several seconds, introducing time lag that causes the sensor to detect the rapid decrease in [O$_2$] within the upper oxycline after descending through this narrow layer (Edwards et al., 2010). Thus, the upper oxycline and the top of the ODZ appear shifted deeper from their true position in the measured profile. This sensor lag also causes $z_{top}$ to be shifted shallower on upcasts as the sensor ascends from the anoxic ODZ core to the upper oxycline. Because most of the CTD profiles used in our analysis contain only downcasts, CTD measurements likely overestimate $z_{top}$ by up to ~30 dbar. Conversely, Argo floats record data during upcasts, meaning that they underestimate $z_{top}$ by at least 6–9.5 m (see Section 2.7).

The uncertainty in $z_{top}$ may be a good estimate for the uncertainty in the depths of all ODZ features. However, the time lag associated with diffusion may vary throughout the water column, as the diffusivity of oxygen in the sensor membrane is a function of temperature and pressure. This membrane is typically made of Teflon or another plastic that contains regions with polymers arranged in amorphous or crystalline phases. Under extreme pressure, the crystalline phase is favored, reducing the membrane's permeability (Natu et al., 2005). This process, and the inclusion of gas molecules in the membrane's polymer matrix (Kapantaidakis et al., 2003), results in a pressure-induced hysteresis effect which causes the [O$_2$] measured by Clark style electrodes to decrease over time (Edwards et al., 2010). Though this may affect the values of d[O$_2$]/dz used to identify ODZ regions, the changes in membrane properties that drive the hysteresis effect occur over several minutes to hours (Kapantaidakis et al., 2003; Natu et al., 2005). Edwards et al. (2010) also observed the greatest declines in measured [O$_2$] at depths greater than 1,000 m, well below the bottom of the ODZ in most parts of the ETNP and ETSP.

### 3.2. STOX Validation of ODZ Detections

The concurrent STOX and CTD casts show that our d[O$_2$]/dz threshold effectively identifies functionally anoxic waters where [O$_2$] is reduced to nanomolar levels (Figure S6a in Supporting Information S1). Where the vertical gradient suggested the presence of anoxia, 90% of STOX [O$_2$] measurements were <0.65 µmol kg$^{-1}$ and 72% were
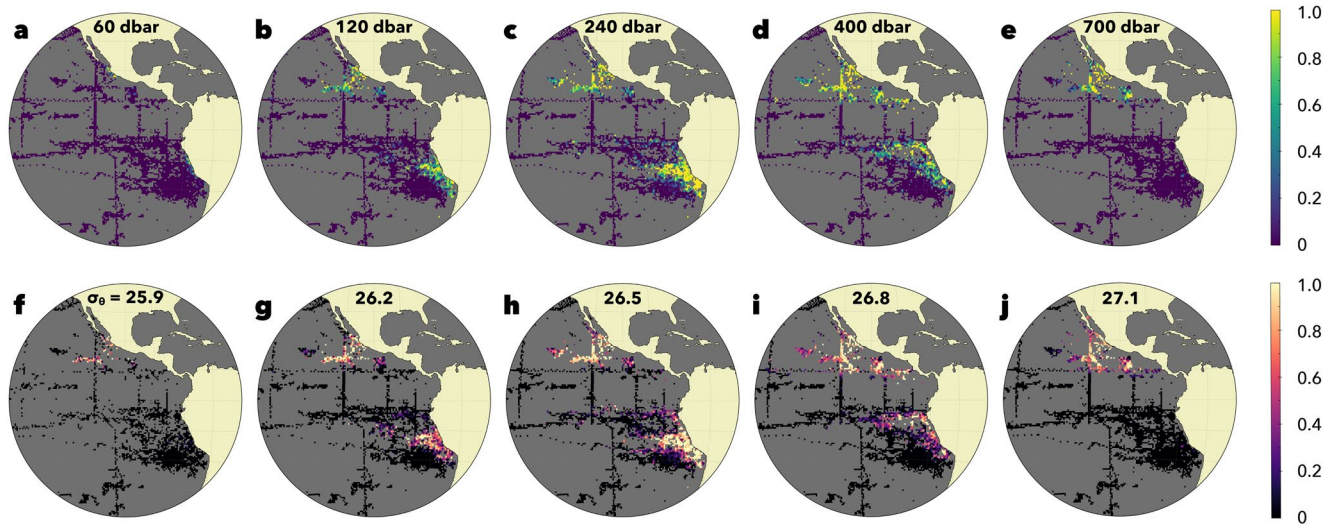
**Figure 2.** Gridded maps of the fraction of measurements identified as ODZ (fODZ) at different (a–e) depths and (f–j) potential densities across the Eastern Tropical Pacific. The gray space in these maps indicates grid cells where no data was available. At 60 dbar, consistently anoxic water is limited to coastal upwelling zones near Mexico and Peru. Anoxia is more widespread in both the ETNP and ETSP at 120, 240, and 400 dbar but present only in the ETNP at 700 dbar. Anoxic water is prevalent only in the ETNP at densities of 25.9 and 27.1 kg m$^{-3}$ but present throughout the ETNP and ETSP at 26.2, 26.5, and 26.8 kg m$^{-3}$.

<0.1 µmol kg$^{-1}$ (Figure S6b in Supporting Information S1). Many of the points in the detected ODZ with STOX O$_2$ greater than these values are near the lower oxycline, consistent with the false ODZ detections in this region that we addressed in Section 2.3. In waters outside of the detected anoxic zone, 77% and 87% of STOX oxygen concentrations were greater than 0.65 and 0.1 µmol kg$^{-1}$ respectively (Figure S6c in Supporting Information S1).

### 3.3. Structure of the ETSP ODZ

The ETSP ODZ's internal structure is well described by the two- and three-dimensional gridded parameters calculated from the data set (Figure 2), and values are summarized in Table 1. On average, the depth of the top of the ODZ is 246 ± 3 dbar (SE) (26.48 ± 0.01 kg m$^{-3}$), with $z_{top}$ ranging from 35 dbar near South America to more than 575 dbar near parts of the ODZ's northern and western margins (Figure 3). The ODZ reaches its shallowest depths between 9° and 14°S and within 0.5° of the Peruvian coast where $z_{top}$ averages 49 ± 5 dbar (26.20 ± 0.02 kg m$^{-3}$). The top of the ODZ is also quite shallow within 5° of the coast and between 9°S and its southern boundary at 24°S (mean $z_{top}$ = 133 ± 3 dbar or 26.031 ± 0.007 kg m$^{-3}$). More than 5° offshore, the top of the ODZ is deeper, occurring at a mean depth of 248 ± 2 dbar (26.492 ± 0.005 kg m$^{-3}$) within this same latitude

**Table 1**
*Summary Statistics of Oxygen Deficient Zones (ODZs) and Comparison to Previous Work*

| Parameter | ETSP | ETNP | Citation |
|---|---|---|---|
| Volume ([O$_2$] < 20 µmol kg$^{-1}$) | 10 ± 9 × 10$^5$ km$^3$ | 5 ± 4 × 10$^6$ km$^3$ | Paulmier and Ruiz-Pino (2009) |
| Volume ([O$_2$] < 20 µmol kg$^{-1}$) | 15–25 × 10$^5$ km$^3$ | 8.8–12 × 10$^6$ km$^3$ | Bianchi et al. (2012) |
| Volume ([O$_2$] < 5 µmol kg$^{-1}$) | 0.4–6.1 × 10$^5$ km$^3$ | 0.6–2.41 × 10$^6$ km$^3$ | Bianchi et al. (2012) |
| Volume (via vertical derivative)[a] | 6.07 ± 0.03 × 10$^5$ km$^3$ (4.5–6.1 × 10$^5$ km$^3$) | 1.93 ± 0.01 × 10$^6$ km$^3$ (1.6–1.9 × 10$^6$ km$^3$) | This study |
| Maximum areal extent[b] | 2.33 ± 0.02 × 10$^6$ km$^2$ | 4.27 ± 0.01 × 10$^6$ km$^2$ | This study |
| Mean thickness | 108 ± 3 dbar (SE) | 286 ± 9 dbar | This study |
| Depth at top of ODZ | 246 ± 3 dbar | 279 ± 6 dbar | This study |
| Density at top of ODZ | 26.48 ± 0.01 kg m$^{-3}$ | 26.48 ± 0.02 kg m$^{-3}$ | This study |

[a]The first value refers to the error from DIVA gridding alone whereas the value in parentheses considers the potential of overestimation from the method misidentifying layers in the lower oxycline as ODZ. [b]From interpolated density layers which, because of the courser 0.1 kg m$^{-3}$ gridding, are based on more data than the 20 dbar wide depth layers. Errors are from DIVA gridding.
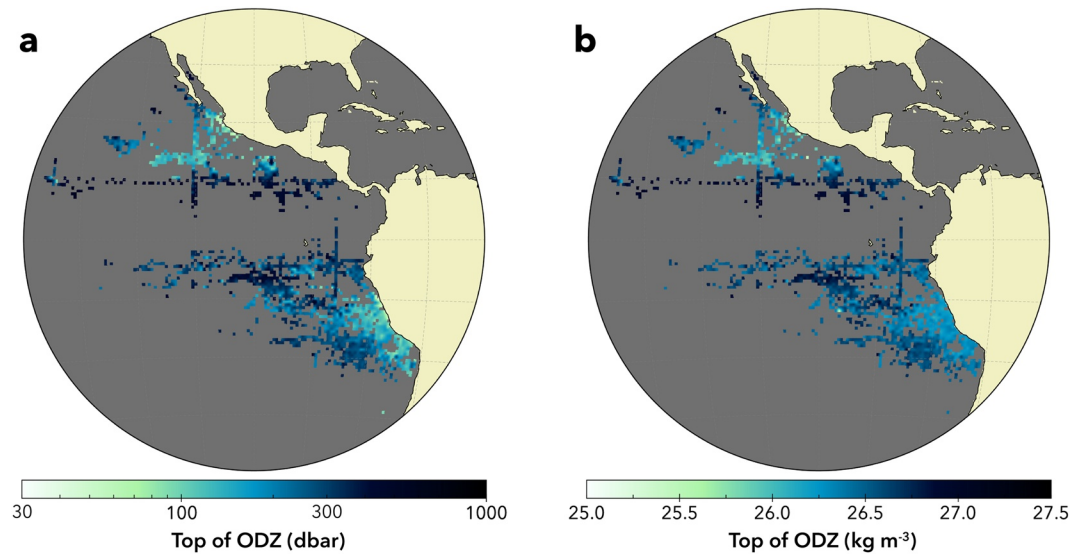
**Figure 3.** Top of the oxygen deficient zone (ODZ), in terms of (a) depth and (b) potential density. Dark gray areas either lacked data or were outside of the ODZ. In both the ETSP and the ETNP, the ODZ reaches shallow depths as low as 35 dbar near upwelling zones off the coasts of Peru and Mexico. The top of the ODZ deepens near the equator in both hemispheres, averaging $321 \pm 4$ dbar (SE) or $26.61 \pm 0.01$ kg m$^{-3}$ between 10°N and 10°S compared to $217 \pm 3$ dbar or $26.40 \pm 0.01$ kg m$^{-3}$ outside of this region.

range. North of 9°S, $z_{top}$ is also deeper, averaging $302 \pm 5$ dbar or $26.57 \pm 0.01$ kg m$^{-3}$ for waters stretching from the South American coast to the westernmost longitude where ODZ was detected (127°W). The ODZ is thickest near South America, with an average thickness of 239 dbar (maximum thickness of 540 dbar) within 5° of the Peruvian coast and between 9° and 17°S (Figure 4). Outside of this region, the ODZ has an average thickness of only 93 dbar (minimum thickness of 20 dbar).
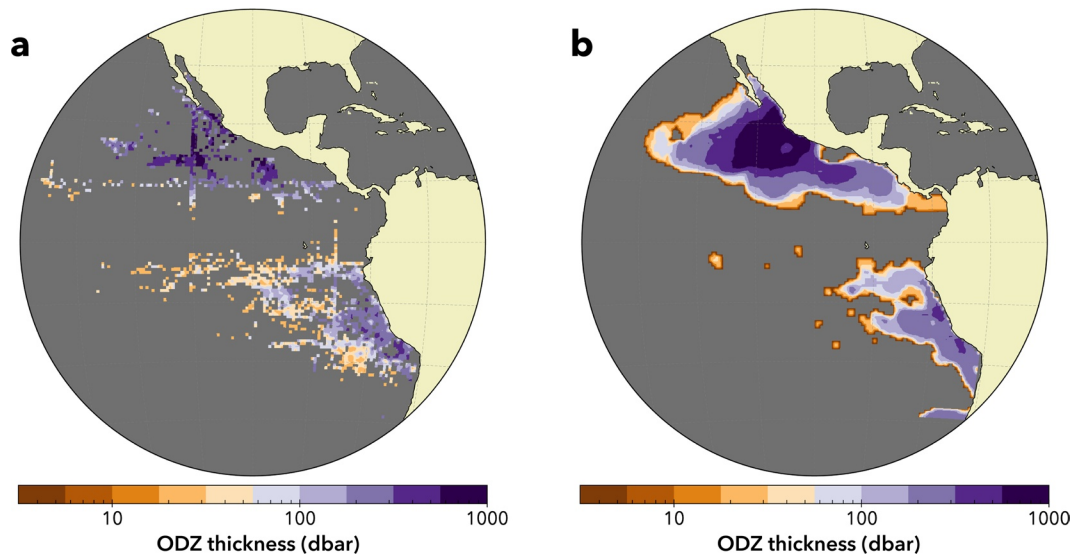


**Figure 4.** Vertical thickness of the oxygen deficient zone (ODZ) calculated from (a) direct observational data or (b) the DIVA interpolation. For (b), the plotted values are the vertical thickness of water with an interpolated fODZ >0.5. In (a), dark gray areas either lacked data or were outside of the ODZ. All thickness values reported here or in Sections 3.2 and 3.3 were calculated using the observational data. In the ETSP, the ODZ is thickest near the Peruvian coast (maximum thickness = 540 dbar) but is only $66 \pm 2$ dbar (SE) thick in waters west of 85°W. The ETNP ODZ is much thicker with an average vertical thickness of $380 \pm 10$ dbar north of 10°N (maximum thickness = 800 dbar). Both ODZs are thinner within 10° of the equator, where the thickness averages $73 \pm 3$ dbar and $104 \pm 7$ dbar in the ETSP and ETNP respectively.
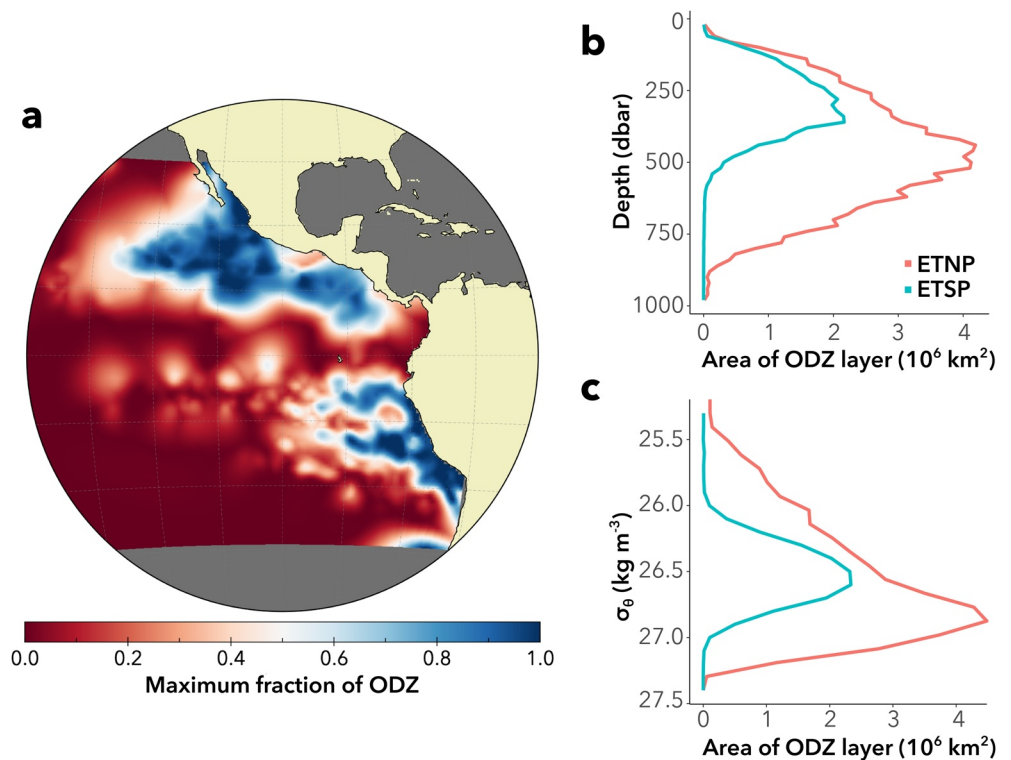
**Figure 5.** (a) Maximum fraction of times a water parcel is identified as part of the oxygen deficient zone (ODZ) as determined from the DIVA interpolations of density surfaces. The horizontal areal extent of anoxic water in each interpolated layer with respect to (b) depth or (c) density of the ETNP (red) and ETSP (teal) ODZs. The ETNP ODZ covers a much larger area than the ETSP ODZ, reaching a maximum areal extent of $4.19 \pm 0.02 \times 10^6$ km$^2$ at depths between 440 and 460 dbar. The ODZ is also most expansive within the 26.9–27.0 kg m$^{-3}$ density layer where it occupies $4.27 \pm 0.01 \times 10^6$ km$^2$ of the Pacific. The ETSP ODZ covers only $2.17 \pm 0.04 \times 10^6$ km$^2$ of the Pacific at depths between 360 and 380 dbar and occupies $2.33 \pm 0.02 \times 10^6$ km$^2$ in waters with densities between 26.6 and 26.7 kg m$^{-3}$.

Sufficient data were available from the ETSP ODZ to interpolate the fraction of ODZ metric (fODZ) and calculate the horizontal extent of anoxic water within a range of depth and density layers (Figure 5). The ETSP ODZ achieves its maximal horizontal extent at depths between 360 and 380 dbar, where it occupies $2.17 \pm 0.03 \times 10^6$ km$^2$ of the ETSP in a region largely between 2° and 20°S and east of 90°W. The ODZ is also most expansive for waters with densities between 26.6 and 26.7 kg m$^{-3}$ where it covers $2.33 \pm 0.02 \times 10^6$ km$^2$. We estimate the ODZ's volume to be $6.07 \pm 0.03 \times 10^5$ km$^3$, similar to the value of $1.0 \pm 0.9 \times 10^6$ km$^3$ reported by Paulmier and Ruiz-Pino (2009) for waters with [O$_2$] < 20 μmol kg$^{-1}$. Our estimate lies at the upper end of the range of volumes calculated by Bianchi et al. (2012) with an [O$_2$] threshold of 5 μmol kg$^{-1}$ ($0.4$–$6.1 \times 10^5$ km$^3$) but is less than their estimates for the volume of water with [O$_2$] < 20 μmol kg$^{-1}$ ($1.5$–$2.5 \times 10^6$ km$^3$). While the Bianchi et al. (2012) estimates attempt to correct for systematic offsets at very low oxygen, our method does not have a similar need. We calculated the small area and volume errors listed above using Equations 2 and 3 respectively. The true error is likely greater than this estimate since the DIVA depth and density layers were interpolated independently. Further, Equation 4 suggests the potential of having overestimated the volume by up to $1.6 \times 10^5$ km$^3$ due to false ODZ detections. Though we cannot account for all sources of error inherent to our approach, this error estimate is more reasonable because it incorporates a known source of uncertainty introduced by our methodology. Nevertheless, our use of the vertical oxygen gradient as a diagnostic parameter for identifying ODZs eliminates much of the error associated with using semi-arbitrary concentration thresholds to approximate anoxia. Here, anoxia refers to oxygen concentrations consumed to a nanomolar subsistence threshold (Revsbech et al., 2009; Zakem & Follows, 2017), not a higher micromolar concentration chosen to offset measurement and interpolation artifacts.

A meridional integration of fODZ in the ETSP (Figure 6) shows that waters where fODZ >0 occur at densities between 25.5 and 27.2 kg m$^{-3}$ and latitudes between 24°S and the equator (Figure 6b). Consistently anoxic waters where fODZ >0.5 are confined to latitudes between 10° and 16°S and potential densities from 26.1 to 26.8 kg
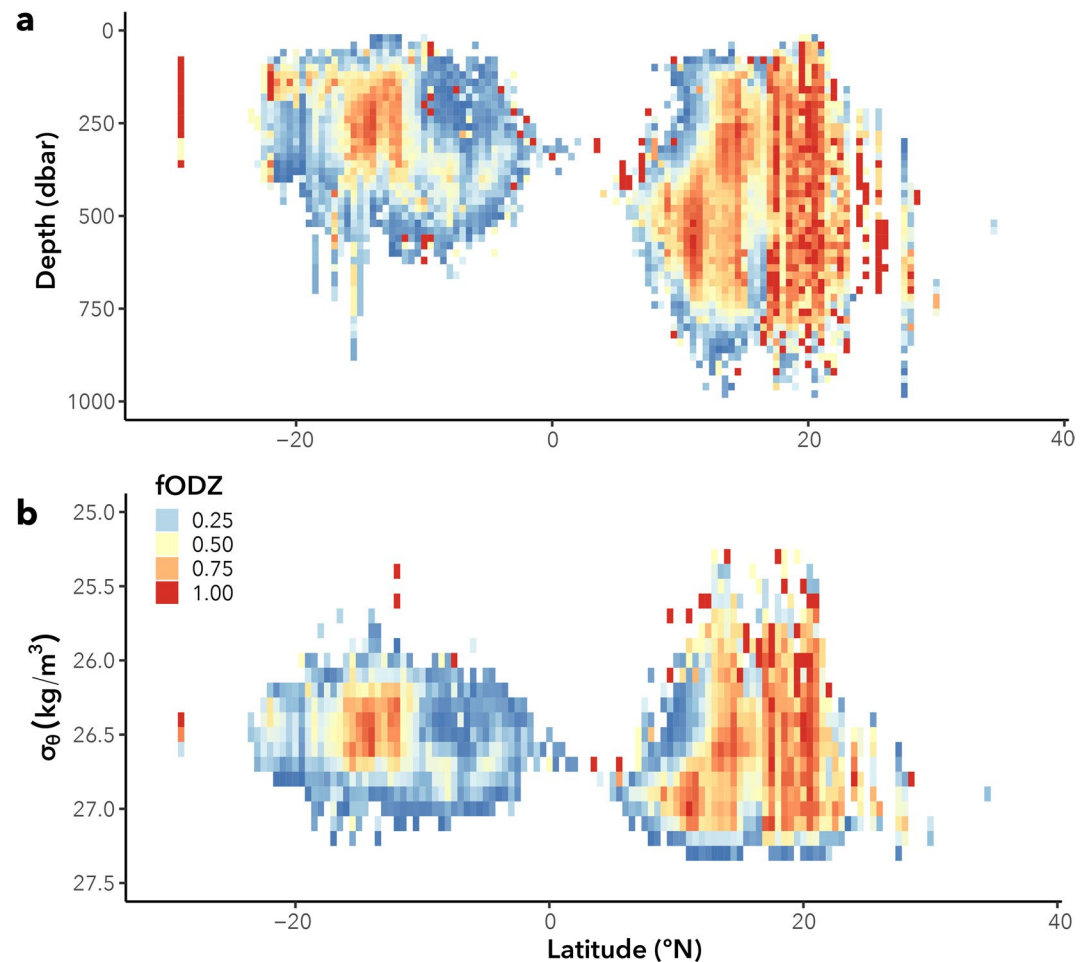
**Figure 6.** Meridional integrations of the fraction of measurements identified as ODZ (fODZ) through the ETNP and ETSP ODZs. The plots show the vertical structure of the ODZs with latitude and depth (a) or potential density (b). To calculate the plotted values of fODZ, we determined the eastern and westernmost longitudes where fODZ >0 at every point shown in the integrations. Then, we computed the total number of observations at each point that fell within this longitude range, as well as the number of observations that were within the ODZ. The displayed values are the number of ODZ points divided by the total number of observations at each point in latitude versus depth or density space. White areas were not sampled or were not part of the ODZ. Both integrations show that the ETSP ODZ contains large regions that are only transiently anoxic where fODZ <0.5. This differs from the ETNP ODZ, where fODZ >0.5 except at the ODZ's edges and in shallow waters near the equator.

m$^{-3}$. This indicates that the ETSP ODZ is well ventilated, containing significant areas of transient anoxia or discontinuous patches of anoxic water. Much of this more ventilated region occurs north of 10°S, where fODZ is elevated at depth but minimal above 360 dbar and 26.7 kg m$^{-3}$. The meridionally integrated values of fODZ shown in Figure 6 are supported by extensive and repeated sampling, as 85% of the grid cells in Figure 6b with fODZ >0 were intersected by at least 10 profiles. A zonal integration of fODZ (Figure S7 in Supporting Information S1) shows that the ETSP ODZ is most intense near the South American coast, with values of fODZ exceeding 0.5 at most locations between the continental margin and 80°W. Zonally integrated fODZ values decrease significantly to the west of this coastal upwelling zone, again indicating the extensive offshore ventilation that gives the ETSP its diffuse structure.

### 3.4. Structure of the ETNP ODZ

The overall extent of the ETNP is shown in Figure 2 and summarized in Table 1. Limited data were available from the ETNP ODZ's northwestern quadrant, the Gulf of California, or the Central American coast. Despite this, the calculated metrics still revealed much about the ODZ's three-dimensional structure. The average depth and

density at the top of the ODZ are $279 \pm 6$ dbar and $26.48 \pm 0.02$ kg m$^{-3}$ respectively. The depth at the top of the ODZ is less than 100 dbar at most sampled locations within 2° of the Mexican coast, especially between 18° and 22°N where significant data were available. Here, $z_{top}$ averages $92 \pm 6$ dbar ($25.95 \pm 0.05$ kg m$^{-3}$) with a minimum value of 42 dbar (25.33 kg m$^{-3}$). The ODZ also reaches shallow depths over much of its interior, with $z_{top}$ averaging $178 \pm 6$ dbar ($26.21 \pm 0.02$ kg m$^{-3}$) for waters between 12° and 22°N and more than 2° west of Mexico. On the east and west coasts of the Baja California peninsula, $z_{top}$ is much deeper, averaging $330 \pm 20$ dbar ($26.65 \pm 0.04$ kg m$^{-3}$) in waters north of 22°N and within 2° of the peninsula. The top of the ODZ is also deeper south of 12°N, where $z_{top}$ is 382 dbar $\pm 7$ dbar ($26.74 \pm 0.01$ kg m$^{-3}$). Here, the ODZ's thickness averages only $155 \pm 8$ dbar, much less than for waters between 10° and 22°N (mean thickness = $420 \pm 10$ dbar, maximum thickness = 800 dbar). The thickness again decreases to the north of this interior region, averaging only $230 \pm 30$ dbar in the sparsely sampled waters surrounding the Baja California peninsula.

Though data were limited, we successfully used the DIVA interpolation of fODZ to estimate the ETNP ODZ's areal extent at different depth and density layers (Figure 5). The ODZ reached its maximum horizontal extent between 440 and 460 dbar where its area was $4.19 \pm 0.02 \times 10^6$ km$^2$. Among the interpolated density layers, the ODZ reached this maximum between 26.9 and 27.0 kg m$^{-3}$ with an area of $4.27 \pm 0.01 \times 10^6$ km$^2$. The ETNP ODZ's volume was estimated as $1.93 \pm 0.01 \times 10^6$ km$^3$, again in agreement with Paulmier and Ruiz-Pino's (2009) estimate of $5 \pm 4 \times 10^6$ km$^3$. Just as for the ETSP, our volume estimate lies near the upper limit of Bianchi et al.'s (2012) calculations for the volume of water with [O$_2$] < 5 µmol kg$^{-1}$ ($0.67$–$2.41 \times 10^6$ km$^3$) and below their estimates using a 20 µmol kg$^{-1}$ threshold ($8.8$–$12.0 \times 10^6$ km$^3$). As in the ETSP, the true error in the volume is likely to be much higher than the value reported above. In fact, our reported volume may be an overestimate by up to $0.29 \times 10^6$ km$^3$ due to false ODZ detections in the lower oxycline.

As shown by meridional and zonal integrations of fODZ in the ETNP (Figure 6 and Figure S8 in Supporting Information S1, respectively), waters with fODZ >0 are generally located between latitudes of 5° and 30°N, longitudes of 80° and 130°W, and potential densities of 25.3 and 27.3 kg m$^{-3}$. Throughout most of this region, fODZ >0.5, indicating that much of the ETNP ODZ is consistently anoxic and not as well ventilated as its ETSP counterpart. Meridionally integrated values of fODZ are less than 0.5 at most locations between 8° and 13°N and with densities between 26.0 and 26.8 kg m$^{-3}$, a region at the southern boundary of the ETNP ODZ. This may reflect ventilation in the southern ETNP by eddies propagating from the Northern Subsurface Countercurrent (NSCC), a process which Margolskee et al. (2019) estimated to account for roughly half of the ETNP ODZ's physical O$_2$ supply. The consistently anoxic waters of the ETNP ODZ also span a wider range of density layers than in the ETSP. However, both ODZs had similar minimum and maximum densities where fODZ >0, suggesting that the water in both hemispheres that is at least transiently anoxic is derived from the same water masses. Further research is needed to characterize the physical processes that ventilate the ETSP ODZ, as differences in the physical oxygen supply to both ODZs may explain why these water masses are more oxygenated in the southern hemisphere. Comparing fODZ with depth for the ETNP and ETSP (Figure S9a in Supporting Information S1) clearly shows the asymmetry in ODZ ventilation between the hemispheres. The values of fODZ are greater in the ETNP than the ETSP, implying that the net oxygen supply, that is, physical oxygen flux minus biological demand, is greater in the ETSP.

### 3.5. Intrusions and Ventilation

Oxygen intrusions were detected throughout the Eastern Pacific ODZs, with higher intrusion rates generally limited to regions with lower values of fODZ (Figure 7). In the ETSP and ETNP, the intrusion rate increases with depth, although not monotonically, before achieving its maximum near the bottom of each ODZ (Figure S9b in Supporting Information S1). These trends suggest that deeper waters are generally better ventilated than those near the ODZ's upper boundary. Despite this overall trend, intrusion rates are elevated near the upper oxycline along the equatorward boundaries of both ODZs (Figures 7 and 8). Between 0° and 10°S, the intrusion rate is highest at a depth of 220 dbar ($26.42 \pm 0.01$ kg m$^{-3}$) and reaches a second smaller maximum at 480 dbar ($26.92 \pm 0.01$ kg m$^{-3}$). In contrast, the intrusion rate maximum occurs at 500 dbar for waters between 10° and 20°S ($26.83 \pm 0.01$ kg m$^{-3}$). Similarly, between 8° and 13°N, the intrusion rate reaches its maximum at a depth of 220 dbar ($26.47 \pm 0.01$ kg m$^{-3}$), shallower than the maximum observed between 13° and 18°N at 440 dbar ($26.85 \pm 0.01$ kg m$^{-3}$) (Figure 8). The reported densities were calculated using linear or quadratic regressions relating depth and potential density within each of the four ODZ subregions ($r^2 \geq 0.97$
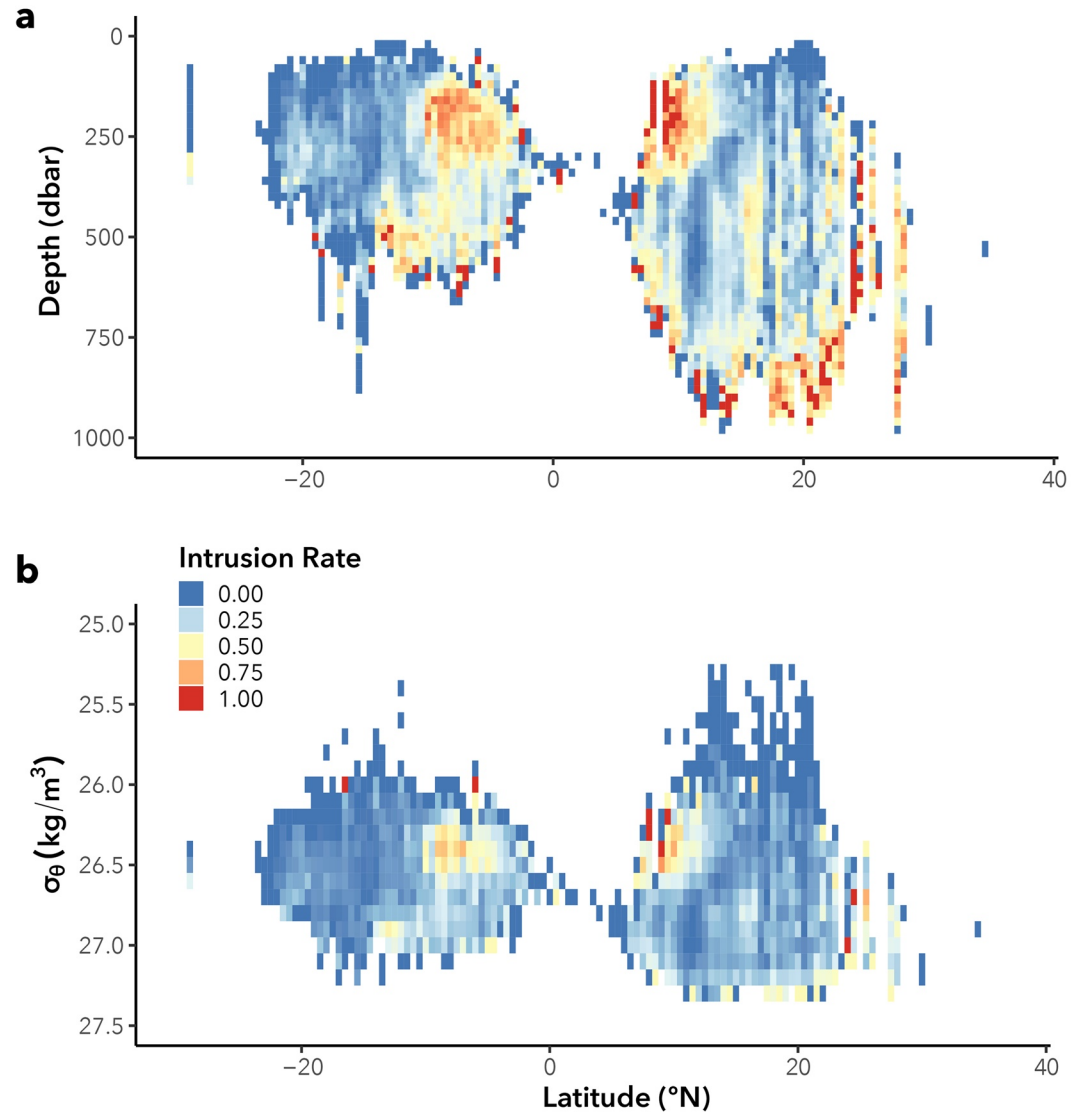
**Figure 7.** Meridional integrations of intrusion rate across the ETNP and ETSP ODZs with (a) depth or (b) potential density as the vertical dimension. The plotted rates were calculated by determining the total number observations that were in intrusions ($n_I$) or the ODZ ($n_{ODZ}$) at every point in latitude versus depth or density space. Meridionally integrated intrusion rates were then calculated from $n_I$ and $n_{ODZ}$ using Equation 5. Intrusions are prevalent near the bottom of the ODZs and at shallower depths near the equator.

for the ETNP subregions and ≥0.86 for the ETSP). We did this to take advantage of the higher resolution of the depth layers when compared to the 0.1 kg m$^{-3}$ thick gridded isopycnals. Errors are 99% confidence intervals.

Our findings regarding intrusions are consistent with Margolskee et al.'s (2019) detection of secondary oxygen maxima near the equatorward boundaries of the ETSP and ETNP ODZs associated with bands of high eddy activity produced by equatorial currents like the Northern Subsurface Countercurrent. These data also show that the ODZs are not homogeneous water masses but instead are ventilated by different mechanisms across different subregions. While eddy activity is important nearer to the equator, deeper advecting water masses ventilate poleward regions of the ODZ. Analyzing intrusion rates or other parameters across the entire ODZ can obscure this and other heterogeneities, highlighting the utility of a high-resolution atlas in resolving the ODZ's complex structure.
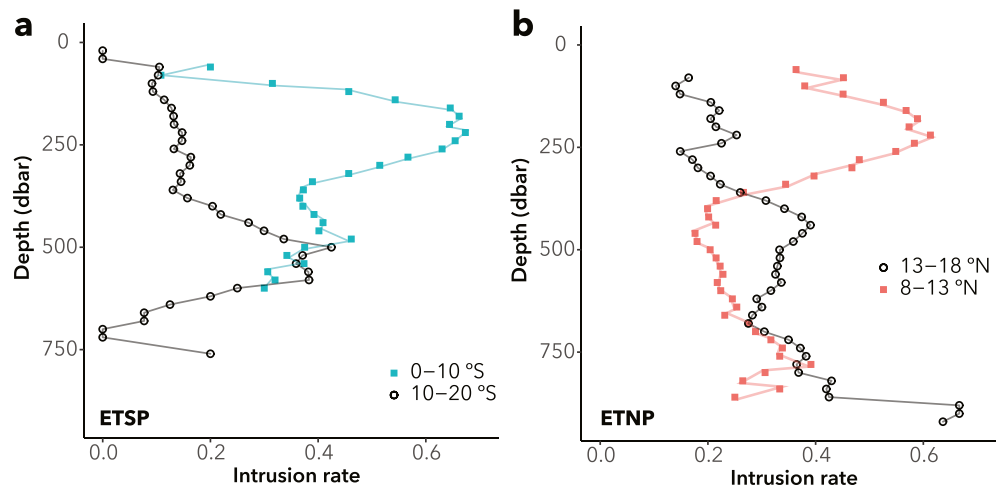
**Figure 8.** Depth profiles of intrusion rate for the (a) ETSP and (b) ETNP ODZs. Intrusion rates within each basin are distinguished by latitude, with the ETSP partitioned between 0°–10°S (teal squares) and 10°–20°S (black circles) and the ETNP between 8°–13°N (red squares) and 13°–18°N (black circles). The different depths where intrusions enter these regions and subregions manifest as local maxima in intrusion rate.

Outside of regions affected by equatorial currents, the intrusion rate is likely reduced at shallower depths due to the steep pycnocline, which limits vertical mixing of oxygen into the upper ODZ. The pycnocline also coincides with higher organic matter flux and a greater biological oxygen demand that prevents the accumulation of oxygen and the formation of detectable intrusions. This demand buffers against allochthonous oxygen supply from surrounding waters, outpacing rates of oxygen transport into the ODZ by eddies or mean advective flow. In regions with intrusions near the surface, especially near the equator, eddies carrying oxygenated water poleward are generated with a sufficient frequency to overcome biological oxygen demand, supporting limited oxygen accumulation in the upper ODZ. Nevertheless, even under these conditions, oxygen intrusions do not penetrate far into the ODZ. Ninety-three percent of grid cells with a nonzero intrusion rate were within 5° or 340 dbar of grid cells with an interpolated fODZ <0.1 (Figure 9).
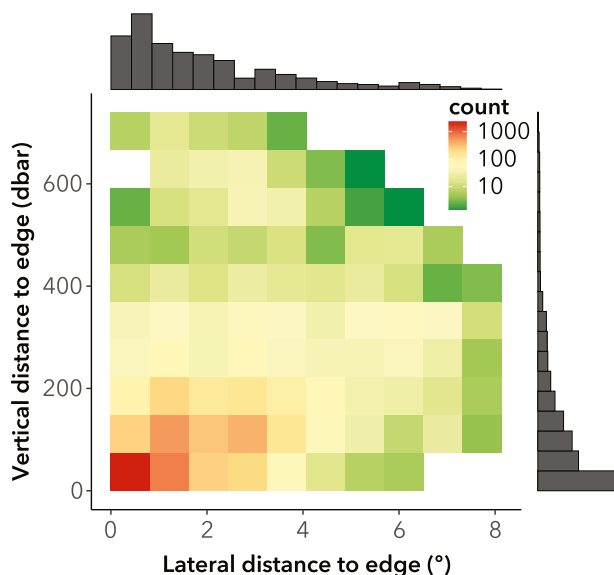
The five intrusion rate maxima highlighted here lie between previously identified water masses that make up or ventilate the Eastern Pacific ODZs. All the maxima are deeper than the 13°C water mass centered at isopycnals of 26.2–26.3 kg m$^{-3}$, which has the lowest oxygen concentrations of any water mass in the Eastern Tropical Pacific (Evans et al., 2020). Further, the deeper local maxima that occur in the poleward reaches of the ODZs are similar in density to the Equatorial Pacific Intermediate Water (EqPIW, 26.7–26.8 kg m$^{-3}$), which forms from subsurface mixing of the Antarctic Intermediate Water, Pacific Deep Water, and other water masses (Bostock et al., 2010; Evans et al., 2020). The small intrusion rate maximum at $\sigma_\theta = 26.92$ kg m$^{-3}$ in equatorial regions of the ETSP is also similar in density to the EqPIW, but such a maximum is not observed in the equatorial ETNP (Figure 8). The EqPIW has O$_2$ concentrations up to 20 μmol L$^{-1}$ in the ETSP (Peters et al., 2018) but as low as nanomolar concentrations in the ETNP (Larsen et al., 2016). Thus, while this water mass may be an importance source of oxygen to the ETSP ODZ, other water masses may produce the deep intrusion rate maximum in the ETNP. Alternatively, the EqPIW may ventilate both ODZs but have a minimal impact on oxygen concentrations in the ETNP given its low [O$_2$] in this region. Either way, these discrepancies contribute to the differences in the ETSP and ETNP ODZs' physical oxygen supply observed in this study.



**Figure 9.** Two-dimensional histogram showing the proximity of oxygen intrusions to the edge of the ODZ. Using the DIVA interpolated depth layers, we calculated the lateral (horizontal) and vertical distances from grid cells with a nonzero intrusion rate to the nearest grid cell with fODZ <0.1. The marginal histograms show the distributions of the horizontal and vertical distances independently whereas the two-dimensional histogram depicts the joint distribution. Ninety-three percent of grid cells with a nonzero intrusion rate were within 5° or 340 dbar of the ODZ's edge.

## 4. Conclusions

We presented a novel method for identifying anoxic water in high resolution sensor-generated oxygen profiles that accounts for calibration offsets between different devices. We applied this method to tens of thousands of oxygen profiles collected from the Eastern Tropical Pacific to produce the most accurate highest resolution three-dimensional atlas of the ETNP and ETSP ODZs to date. The atlas shows the ODZ at a much higher level of detail than could be achieved using oxygen climatologies based on discretized measurements, locating both the depths of maximal ODZ extent as well as the consistent oxygen intrusions ventilating the ODZs at their boundaries. This data product is available to be utilized by oceanographers to validate oxygen resolving models and analyze the physical and biological mechanisms that give rise to ODZs and shape the Eastern Pacific's oxygen distribution. This framework can be harnessed into the future to monitor the vertical and horizontal extent of anoxic waters, as well as to quantify the impact and consistency of mesoscale features that give the ODZs their irregular and complex shape. This data set acts as a baseline against which future oxygen measurement can be compared to evaluate whether the ODZs are shoaling and expanding laterally due to climate change, and to consider their impact on budgets like nitrous oxide (Babbin et al., 2020; Codispoti, 2010). However, to be robust, future oxygen measurements must maintain and report a higher (meter scale) vertical resolution than is widely available today.

## Data Availability Statement

Gridded data are available through BCO-DMO (https://doi.org/10.26008/1912/bco-dmo.865316.1) and are included as Supporting Information S1. The original data are freely available at the Argo (http://www.argodatamgt.org), R2R (https://www.rvdata.us/), and CCHDO (https://cchdo.ucsd.edu/) online repositories.

## References

Arévalo-Martínez, D. L., Kock, A., Löscher, C. R., Schmitz, R. A., & Bange, H. W. (2015). Massive nitrous oxide emissions from the tropical South Pacific Ocean. *Nature Geoscience*, 8(7), 530–533. https://doi.org/10.1038/ngeo2469

Argo Data Management Team. (2021). *Argo user's manual V3.4*. Ifremer. https://doi.org/10.13155/29825

Babbin, A. R., Bianchi, D., Jayakumar, A., & Ward, B. B. (2015). Rapid nitrous oxide cycling in the suboxic ocean. *Science*, 348(6239), 1127–1129. https://doi.org/10.1126/science.aaa8380

Babbin, A. R., Boles, E. L., Mühle, J., & Weiss, R. F. (2020). On the natural spatio-temporal heterogeneity of South Pacific nitrous oxide. *Nature Communications*, 11(1), 3672. https://doi.org/10.1038/s41467-020-17509-6

Beckers, J.-M., Barth, A., Troupin, C., & Alvera-Azcárate, A. (2014). Approximate and efficient methods to assess error fields in spatial gridding with data interpolating variational analysis (DIVA). *Journal of Atmospheric and Oceanic Technology*, 31(2), 515–530. https://doi.org/10.1175/JTECH-D-13-00130.1

Bianchi, D., Dunne, J. P., Sarmiento, J. L., & Galbraith, E. D. (2012). Data-based estimates of suboxia, denitrification, and $N_2O$ production in the ocean and their sensitivities to dissolved $O_2$. *Global Biogeochemical Cycles*, 26(2). https://doi.org/10.1029/2011GB004209

Bittig, H. C., & Körtzinger, A. (2015). Tackling oxygen optode drift: Near-surface and in-air oxygen optode measurements on a float provide an accurate in situ reference. *Journal of Atmospheric and Oceanic Technology*, 32(8), 1536–1543. https://doi.org/10.1175/JTECH-D-14-00162.1

Bittig, H. C., & Körtzinger, A. (2017). Technical note: Update on response times, in-air measurements, and in situ drift for oxygen optodes on profiling platforms. *Ocean Science*, 13(1), 1–11. https://doi.org/10.5194/os-13-1-2017

Bittig, H. C., Körtzinger, A., Neill, C., van Ooijen, E., Plant, J. N., Hahn, J., et al. (2018). Oxygen optode sensors: Principle, characterization, calibration, and application in the ocean. *Frontiers in Marine Science*, 4. https://doi.org/10.3389/fmars.2017.00429

Bostock, H. C., Opdyke, B. N., & Williams, M. J. M. (2010). Characterising the intermediate depth waters of the Pacific Ocean using $\delta^{13}C$ and other geochemical tracers. *Deep Sea Research Part I: Oceanographic Research Papers*, 57(7), 847–859. https://doi.org/10.1016/j.dsr.2010.04.005

Brandes, J. A., & Devol, A. H. (2002). A global marine-fixed nitrogen isotopic budget: Implications for Holocene nitrogen cycling. *Global Biogeochemical Cycles*, 16(4), 67-1–67-14. https://doi.org/10.1029/2001GB001856

Breitburg, D., Levin, L. A., Oschlies, A., Grégoire, M., Chavez, F. P., Conley, D. J., et al. (2018). Declining oxygen in the global ocean and coastal waters. *Science*, 359(6371). https://doi.org/10.1126/science.aam7240

Bristow, L. A., Callbeck, C. M., Larsen, M., Altabet, M. A., Dekaezemacker, J., Forth, M., et al. (2017). $N_2$ production rates limited by nitrite availability in the Bay of Bengal oxygen minimum zone. *Nature Geoscience*, 10(1), 24–29. https://doi.org/10.1038/ngeo2847

Bristow, L. A., Dalsgaard, T., Tiano, L., Mills, D. B., Bertagnolli, A. D., Wright, J. J., et al. (2016). Ammonium and nitrite oxidation at nanomolar oxygen concentrations in oxygen minimum zone waters. *Proceedings of the National Academy of Sciences*, 113(38), 10601–10606. https://doi.org/10.1073/pnas.1600359113

Bushinsky, S. M., Emerson, S. R., Riser, S. C., & Swift, D. D. (2016). Accurate oxygen measurements on modified Argo floats using in situ air calibrations. *Limnology and Oceanography: Methods*, 14(8), 491–505. https://doi.org/10.1002/lom3.10107

Cabré, A., Marinov, I., Bernardello, R., & Bianchi, D. (2015). Oxygen minimum zones in the tropical Pacific across CMIP5 models: Mean state differences and climate change trends. *Biogeosciences*, 12(18), 5429–5454. https://doi.org/10.5194/bg-12-5429-2015

Codispoti, L. A. (2010). Interesting times for marine $N_2O$. *Science*, 327(5971), 1339–1340. https://doi.org/10.1126/science.1184945

Dalsgaard, T., Stewart, F. J., Thamdrup, B., Brabandere, L. D., Revsbech, N. P., Ulloa, O., et al. (2014). Oxygen at nanomolar levels reversibly suppresses process rates and gene expression in anammox and denitrification in the oxygen minimum zone off northern Chile. *MBio*, 5(6), e01966-14. https://doi.org/10.1128/mBio.01966-14

DeVries, T., Deutsch, C., Rafter, P. A., & Primeau, F. (2013). Marine denitrification rates determined from a global 3-D inverse model. *Biogeosciences*, 10(4), 2481–2496. https://doi.org/10.5194/bg-10-2481-2013

Edwards, B., Murphy, D., Janzen, C., & Larson, N. (2010). Calibration, response, and hysteresis in deep-sea dissolved oxygen measurements. *Journal of Atmospheric and Oceanic Technology*, *27*(5), 920–931. https://doi.org/10.1175/2009JTECHO693.1

Evans, N., Boles, E., Kwiecinski, J. V., Mullen, S., Wolf, M., Devol, A. H., et al. (2020). The role of water masses in shaping the distribution of redox active compounds in the Eastern Tropical North Pacific oxygen deficient zone and influencing low oxygen concentrations in the eastern Pacific Ocean. *Limnology and Oceanography*, *65*(8), 1688–1705. https://doi.org/10.1002/lno.11412

Farías, L., Castro-González, M., Cornejo, M., Charpentier, J., Faúndez, J., Boontanon, N., & Yoshida, N. (2009). Denitrification and nitrous oxide cycling within the upper oxycline of the eastern tropical South Pacific oxygen minimum zone. *Limnology and Oceanography*, *54*(1), 132–144. https://doi.org/10.4319/lo.2009.54.1.0132

Garcia, H. E., Weathers, K. W., Paver, C. R., Smolyar, I., Boyer, T. P., Locarnini, R. A., et al. (2019). World ocean atlas 2018, volume 3: Dissolved oxygen, apparent oxygen utilization, and oxygen saturation. *NOAA Atlas NESDIS*, *83*.

Garcia-Robledo, E., Padilla, C. C., Aldunate, M., Stewart, F. J., Ulloa, O., Paulmier, A., et al. (2017). Cryptic oxygen cycling in anoxic marine zones. *Proceedings of the National Academy of Sciences*, *114*(31), 8319–8324. https://doi.org/10.1073/pnas.1619844114

IOC, SCOR, & IAPSO. (2010). *The International thermodynamic equation of seawater – 2010: Calculation and use of thermodynamic properties* (Report No. 56). Intergovernmental Oceanographic Commission, Manuals and Guides No. 56, UNESCO.

Ito, T., & Deutsch, C. (2013). Variability of the oxygen minimum zone in the tropical North Pacific during the late twentieth century. *Global Biogeochemical Cycles*, *27*(4), 1119–1128. https://doi.org/10.1002/2013GB004567

Johnson, K. S., Plant, J. N., Riser, S. C., & Gilbert, D. (2015). Air oxygen calibration of oxygen optodes on a profiling float array. *Journal of Atmospheric and Oceanic Technology*, *32*(11), 2160–2172. https://doi.org/10.1175/JTECH-D-15-0101.1

Johnson, K. S., Riser, S. C., & Ravichandran, M. (2019). Oxygen variability controls denitrification in the Bay of Bengal oxygen minimum zone. *Geophysical Research Letters*, *46*(2), 804–811. https://doi.org/10.1029/2018GL079881

Kapantaidakis, G., Koops, G., Wessling, M., Kaldis, S., & Sakellaropoulos, G. (2003). $CO_2$ Plasticization of polyethersulfone/polyimide gas-separation membranes. *AIChE Journal*, *49*, 1702–1711. https://doi.org/10.1002/aic.690490710

Karstensen, J., Stramma, L., & Visbeck, M. (2008). Oxygen minimum zones in the eastern tropical Atlantic and Pacific oceans. *Progress in Oceanography*, *77*(4), 331–350. https://doi.org/10.1016/j.pocean.2007.05.009

Larsen, M., Lehner, P., Borisov, S. M., Klimant, I., Fischer, J. P., Stewart, F. J., et al. (2016). In situ quantification of ultra-low $O_2$ concentrations in oxygen minimum zones: Application of novel optodes. *Limnology and Oceanography: Methods*, *14*(12), 784–800. https://doi.org/10.1002/lom3.10126

Margolskee, A., Frenzel, H., Emerson, S., & Deutsch, C. (2019). Ventilation pathways for the North Pacific oxygen deficient zone. *Global Biogeochemical Cycles*, *33*(7), 875–890. https://doi.org/10.1029/2018GB006149

McDougall, T., & Barker, P. M. (2011). Getting started with TEOS-10 and the Gibbs Seawater (GSW) oceanographic toolbox. *SCOR/IAPSO WG*, *127*, 1–28.

Muggeo, V. (2008). Segmented: An R package to fit regression models with broken-line relationships. *R News*, *8*, 20–25.

Natu, A. A., Lofgren, E. A., & Jabarin, S. A. (2005). Effect of morphology on barrier properties of poly(ethylene terephthalate). *Polymer Engineering & Science*, *45*(3), 400–409. https://doi.org/10.1002/pen.20288

Paulmier, A., & Ruiz-Pino, D. (2009). Oxygen minimum zones (OMZs) in the modern ocean. *Progress in Oceanography*, *80*(3–4), 113–128. https://doi.org/10.1016/j.pocean.2008.08.001

Peters, B. D., Jenkins, W. J., Swift, J. H., German, C. R., Moffett, J. W., Cutter, G. A., et al. (2018). Water mass analysis of the 2013 US GEOTRACES eastern Pacific zonal transect (GP16). *Marine Chemistry*, *201*, 6–19. https://doi.org/10.1016/j.marchem.2017.09.007

Revsbech, N. P., Larsen, L. H., Gundersen, J., Dalsgaard, T., Ulloa, O., & Thamdrup, B. (2009). Determination of ultra-low oxygen concentrations in oxygen minimum zones by the STOX sensor. *Limnology and Oceanography: Methods*, *7*(5), 371–381. https://doi.org/10.4319/lom.2009.7.371

Schmidtko, S., Stramma, L., & Visbeck, M. (2017). Decline in global oceanic oxygen content during the past five decades. *Nature*, *542*(7641), 335–339. https://doi.org/10.1038/nature21399

Stramma, L., Johnson, G. C., Sprintall, J., & Mohrholz, V. (2008). Expanding oxygen-minimum zones in the tropical oceans. *Science*, *320*(5876), 655–658. https://doi.org/10.1126/science.1153847

Thamdrup, B., Dalsgaard, T., & Revsbech, N. P. (2012). Widespread functional anoxia in the oxygen minimum zone of the Eastern South Pacific. *Deep Sea Research Part I: Oceanographic Research Papers*, *65*, 36–45. https://doi.org/10.1016/j.dsr.2012.03.001

Tiano, L., Garcia-Robledo, E., Dalsgaard, T., Devol, A. H., Ward, B. B., Ulloa, O., et al. (2014). Oxygen distribution and aerobic respiration in the north and south eastern tropical Pacific oxygen minimum zones. *Deep Sea Research Part I: Oceanographic Research Papers*, *94*, 173–183. https://doi.org/10.1016/j.dsr.2014.10.001

Troupin, C., Barth, A., Sirjacobs, D., Ouberdous, M., Brankart, J.-M., Brasseur, P., et al. (2012). Generation of analysis and consistent error fields using the Data Interpolating Variational Analysis (DIVA). *Ocean Modelling*, *52*(53), 90–101. https://doi.org/10.1016/j.ocemod.2012.05.002

Troupin, C., Ouberdous, M., Sirjacobs, D., Alvera-Azcárate, A., Barth, A., Toussaint, M.-E., et al. (2013). *Diva user guide*. Retrieved from http://modb.oce.ulg.ac.be/mediawiki/index.php/Diva_documents

Uchida, H., Johnson, G. C., & McTaggart, K. E. (2010). CTD oxygen sensor calibration procedures. In *The GO-SHIP repeat hydrography manual: A collection of expert reports and guidelines*. IPCCP Report No. 14, ICPO Publication Series No. 134, Version 1.

Wong, A. P. S., Wijffels, S. E., Riser, S. C., Pouliquen, S., Hosoda, S., Roemmich, D., et al. (2020). Argo data 1999–2019: Two million temperature-salinity profiles and subsurface velocity observations from a global array of profiling floats. *Frontiers in Marine Science*, *7*, 700. https://doi.org/10.3389/fmars.2020.00700

Wong, G. T. F., & Li, K.-Y. (2009). Winkler's method overestimates dissolved oxygen in seawater: Iodate interference and its oceanographic implications. *Marine Chemistry*, *115*, 86–91. https://doi.org/10.1016/j.marchem.2009.06.008

Zakem, E. J., & Follows, M. J. (2017). A theoretical basis for a nanomolar critical oxygen concentration. *Limnology and Oceanography*, *62*(2), 795–805. https://doi.org/10.1002/lno.10461